PAPER

Check for updates

Atmospheric pressure chemical vapor deposition of methylammonium bismuth iodide thin films†

Xiao Chen, [ID] ‡[a] Yoon Myung,[ab] Arashdeep Thind, [ID] [c] Zhengning Gao, [ID] [c] Bo Yin,[c] Meikun Shen,[d] Sung Beom Cho,[a] Peifu Cheng,[a] Bryce Sadtler, [ID] [cd] Rohan Mishra [ID] [ac] and Parag Banerjee [ID] *[ac]

We demonstrate the atmospheric pressure chemical vapor deposition of methyl ammonium bismuth iodide ($(CH_3NH_3)_3Bi_2I_9$ or $MA_3Bi_2I_9$) films. $MA_3Bi_2I_9$ possesses an indirect optical bandgap of 1.80 eV and a room temperature excitonic peak at 511 nm. In contrast to recent reports, the films are n-type semiconductors with a room temperature carrier concentration of 3.36×10^{18} cm^{-3} and a Hall mobility of 18 cm^2 V^{-1} s^{-1}, which are superior to those of solution-processed, undoped films. The precursors used for the deposition are methylammonium iodide and bismuth iodide which are co-sublimated at 199 °C and 230 °C, respectively, in an Ar flow inside a tube furnace with a variable temperature profile. The substrate temperature is set at 160 °C, and dense polycrystalline films (~775 nm thick) are deposited. Extensive characterization combined with first-principles density functional theory calculations unravels the synthesis–structure–property relationship in these films. The degradation of properties under ambient conditions results from film oxidation with a characteristic bi-exponential decay in resistivity, signifying a fast surface oxidation followed by a slower oxidation of the bulk.

1 Introduction

Lead halide perovskites ($CH_3NH_3PbI_3$ or $MAPbI_3$ and its variants) are promising solar-cell absorber materials with reported power conversion efficiencies that have rapidly increased from[1] 3.8% in 2009 to an impressive[2] 22.1% in 2017. The fundamental material properties of lead halide perovskites that drive such progress are their high charge-carrier mobilities,[3] high optical absorption coefficient,[4] ideal and tunable bandgap[5] and ultra-long carrier diffusion lengths up to a few microns.[3,6,7]

Though the reported power conversion efficiencies of lead halide perovskite solar cells are now competitive with those of commercial silicon solar cells, there are two limitations preventing the commercialization of such solar cells.[8] They are (1) the environmental, device and thermodynamic instability[9,10] of the perovskites in the presence of air, humidity, light and

electric fields; and (2) the toxicity[11] due to the presence of lead. Attempts to address stability limitations have included replacing the A-site organic component ($CH_3NH_3^+$) with inorganic cations,[12,13] such as Cs^+ and Rb^+, or by providing protective overlayers[14] that prevent the exposure of lead halide perovskite films to ambient conditions. However, the toxicity due to the presence of lead in these perovskites presents a challenge to further scale-up and eventual commercialization.

Recently, bismuth[15–17] (Bi^{3+}) has drawn attention[18] as a substituent to the B-site occupied by Pb^{2+} for 'lead-free' perovskites,[19] since it is a non-toxic 6p-block element that is isoelectronic[20–22] with Pb^{2+}. Reports on the promising optoelectronic and photovoltaic properties of methylammonium bismuth iodide (with the formula unit ($CH_3NH_3)_3Bi_2I_9$ and henceforth called $MA_3Bi_2I_9$) with a high absorption coefficient[23] and long term stability[24] have been published. However, $MA_3Bi_2I_9$ based solar cells suffer from low efficiency.[25] Besides the sub-optimal electronic structure of $MA_3Bi_2I_9$ compared to $MAPbI_3$,[17,26] the diminished performance of the solar cells is also attributed to the commonly used solution deposition techniques that result in a poor morphology, purity and coverage of the films on substrates.[27,28]

Thus in this article, we demonstrate a gas-phase deposition technique for $MA_3Bi_2I_9$ thin films using a low temperature (160 °C), atmospheric pressure chemical vapor deposition (APCVD) process. We obtain films with better control over the morphology, purity and coverage with the added advantage of rapid scale-up and integration with other solar manufacturing processes. The APCVD process occurs in a tube furnace by taking advantage of the

[a]Department of Mechanical Engineering and Materials Science, Washington University in St. Louis, St. Louis, MO-63130, USA. E-mail: parag.banerjee@wustl.edu

[b]Department of Nanotechnology and Advanced Materials Engineering, Sejong University, Seoul, 05006, Korea

[c]Institute of Materials Science & Engineering, Washington University in St. Louis, St. Louis, MO-63130, USA

[d]Department of Chemistry, Washington University in St. Louis, St. Louis, MO-63130, USA

† Electronic supplementary information (ESI) available. See DOI: 10.1039/c7ta06578g

‡ Current address: Suzhou Institute of Nano-Tech and Nano-Bionics, Chinese Academy of Sciences, Suzhou, 215123, P. R. China.

variable temperature gradient along the length of the tube. Specific temperature zones within the tube are utilized to co-sublimate methylammonium iodide (with the chemical formula unit CH_3NH_3I and henceforth referred to as MAI) and bismuth iodide (BiI_3) into vapor form, which condenses and reacts on the cooler, downstream side of the tube furnace. The result is an n-type, dense and polycrystalline $MA_3Bi_2I_9$ film with an optical bandgap of 1.80 eV, a room-temperature free electron carrier density of 3.36×10^{18} cm^{-3} and a Hall mobility of 18 cm^2 V^{-1} s^{-1}. We discuss the synthesis–structure–property interrelationship in $MA_3Bi_2I_9$ films obtained from a suite of characterization techniques and first-principles density functional theory (DFT) calculations.

2 Experimental

2.1 Methylammonium iodide preparation

Methylammonium iodide (MAI) was synthesized using minor modifications to a previously published procedure.[29] First, 25 mL of methylamine (33 wt% in ethanol, Sigma-Aldrich) was added to a 250 mL, three-neck flask maintained at a temperature lower than 7 °C. 10 mL of hydroiodic acid (HI, 57 wt% in water, Sigma-Aldrich) was added dropwise to the flask at a rate of approximately 6 drops per 10 s to the MAI solution while the solution was stirred at 300 rpm. The white MAI precipitate was recovered from the solution using rotary evaporation at a pressure of 60 Torr with the flask in a water bath at 50 °C.

The collected MAI powder was dissolved in 10 mL absolute ethanol while stirring and sonicating for 10 minutes and then precipitated by adding 50–55 mL of diethyl ether to the solution and refrigerating it for 20 minutes. After filtration, the process was repeated 3 times, and finally a white powder was obtained and dried at 60 °C overnight under vacuum using a Schlenk

line. The phase purity of the compound was confirmed by using a Bruker D8 Advance powder X-ray diffractometer (ESI S1†).

2.2 $MA_3Bi_2I_9$ thin film synthesis *via* APCVD

The MAI powder prepared above was used as the first precursor for the APCVD. BiI_3 powder (99%, Aldrich) was used as the second precursor for the APCVD without further purification. A quartz tube mounted on a single zone furnace (Compact Split Tube Furnace with a 1″ Tube-OTF-1200X-S, MTI Corporation) was used for all APCVD studies. Silicon wafers (Test Grade, University Wafers Inc.) with or without a 100 nm thermal oxide layer, glass slides (48300-025, VWR), pre-cut 5 mm × 5 mm high purity quartz substrates (MTI Corporation) and 2 cm × 2 cm Willow® flexible glass from Corning were used as substrates. The silicon and glass substrates were cut into an approximately 1 cm × 2 cm size, ultrasonically cleaned in DI water, acetone (99.9% Aldrich) and ethanol (99.9% Aldrich) mixture for 10 minutes, washed with IPA and DI water, dried in compressed air, cleaned in UV Ozone (Ossila E511) for 10 minutes, and then immediately placed in the quartz tube, 23 cm away from the upstream end.

The schematic of the experimental set-up is shown in Fig. 1a, while a picture of the furnace after successful $MA_3Bi_2I_9$ deposition is shown in Fig. 1b. The deposition is marked by the characteristic orange color of the $MA_3Bi_2I_9$ film on the downstream side.[15] Initially, 50 mg of MAI and 60 mg of BiI_3 were used as sources and placed at 2.5 cm and 13 cm from the upstream end of the quartz tube in alumina boat crucibles. First, the quartz tube was purged with a 280 standard cubic centimeters per minute (sccm) flow of ultra-high purity Ar gas (UHP 300, Airgas) for 10 minutes. The temperature in the quartz tube was then raised at a rate of 1.8 °C per minute until the temperature at the center of the tube reached 230 °C. The
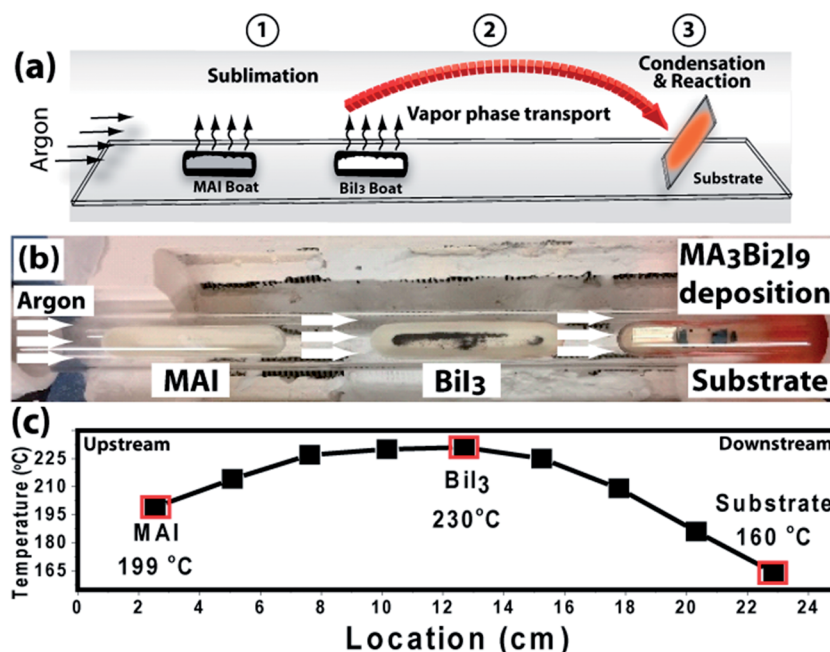

Fig. 1 (a) Schematic of APCVD for $MA_3Bi_2I_9$ thin films, (b) image of MAI and BiI_3 boats inside the tube furnace, and (c) temperature profile of the tube furnace showing the MAI and BiI_3 sublimation temperatures and $MA_3Bi_2I_9$ film deposition temperature.

Table 1 The partial pressures obtained from thermogravimetric analysis of MAI and BiI_3 powders. MAI and BiI_3 vapor pressures were calculated at their sublimation temperatures of 199 °C and 230 °C, respectively. The ratio of MAI : BiI_3 vapor pressures is 4.7 : 1. Similarly, at the point of condensation where the temperature is 160 °C, the ratio of MAI : BiI_3 vapor pressures was 87 : 1, indicating a far higher driving force for BiI_3 to condense, nucleate and grow

	Precursor compound	Process	Temperature (°C)	Partial pressure	MAI : BiI_3 ratio	
					Sublimation	Deposition
1	MAI	Sublimation	199 °C	0.0846	4.7 : 1	
2	BiI_3	Sublimation	230 °C	0.0180		
3	MAI	Deposition	160 °C	0.01133		87 : 1
4	BiI_3	Deposition	160 °C	0.00013		

furnace was maintained at this temperature for various time periods of 15, 30, 45, 60, 90, 180, 240, 360 and 480 minutes of deposition. After deposition, the furnace was naturally allowed to cool down to ambient temperature. This usually took 3 hours.

The key aspect of an APCVD process lies in the precise placement of the MAI and BiI_3 sources along the length of the quartz furnace reactor. This allows us to co-sublimate both the sources together. Fig. 1c shows the temperature profile of the furnace along the length of the CVD quartz tube. This calibration measurement was done prior to the deposition by sliding a thermocouple probe inserted inside the quartz tube with Ar flowing at a rate of 280 sccm. The temperature varies from 199 °C from the upstream end (labeled as 2.5 cm on the x-axis) and peaks to the desired temperature set-point of the furnace (230 °C) at the center of the tube (13 cm from the upstream end). The temperature then drops on the downstream side to 160 °C, 23 cm from the upstream end.

The variability of the temperature along the length of the quartz furnace reactor is exploited in the APCVD process. The MAI boat is placed at 2.5 cm from the upstream side where temperature is 199 °C which allows the MAI to sublimate. We note that MAI has a melting point of 270 °C. The BiI_3 is kept in the middle of the quartz reactor where the temperature is 230 °C. BiI_3 has a melting point[30] of 402 °C but is known to sublimate as well. Thus, the Ar flow causes the simultaneous transport of MAI and BiI_3 vapors to the cooler zone in the downstream region. The condensation and reaction of the MAI and BiI_3 vapors take place to produce a $MA_3Bi_2I_9$ film at around 23 cm from the upstream side, where the temperature is maintained at 160 °C.

Thermogravimetric measurements have been used to calculate the vapor pressure of the two precursors, MAI and BiI_3. The details of this analysis are provided in ESI S2.† The enthalpy of sublimation of MAI is obtained from Dualeh *et al.*,[31] as 105 ± 5 kJ mol^{-1}, and for BiI_3 it is estimated in this work to be 128 ± 2 kJ mol^{-1}. The sublimation temperatures (T_{sub}) at atmospheric pressure for MAI and BiI_3 are found to be 247 ± 26 °C and 316 ± 2 °C, respectively. Based on this analysis, the partial pressure of MAI and BiI_3 when the total pressure is 760 Torr, at the points of sublimation and deposition, has been calculated. The vapor pressure as a function of temperature is provided in Table 1. At the points of sublimation (199 °C for MAI and 230 °C for BiI_3), it can be seen that the partial pressure of MAI is higher than that

of BiI_3 by 4.7×. As the vapor moves downstream, the temperature drops and at 160 °C (*i.e.*, the deposition temperature), the MAI vapor pressure is 87× higher than that of BiI_3. Furthermore, the thermodynamic driving force for condensation which is given as[32] $\Delta G|_{gas \to solid} = -(\Delta H_{sub}) \times \dfrac{(T_{sub} - T)}{T_{sub}}$ is found to be -17.57 kJ mol^{-1} for MAI but -33.9 kJ mol^{-1} for BiI_3 using data from ESI S2.† Here, T is the deposition temperature where, $T = 160$ °C. This implies that the BiI_3 should readily condense on the substrate, nucleate and grow. On the other hand, MAI condensation followed by a solid-state reaction with BiI_3 to form $MA_3Bi_2I_9$ may be a kinetically rate determining step for $MA_3Bi_2I_9$ film formation. Evidence of this effect will be presented in the Results & discussion section.

2.3 Film characterization

The film morphology was characterized by using a JEOL JSM-7001 LVF Field Emission SEM under an accelerating voltage of 10 kV. X-ray diffraction (2θ scans) of the deposited $MA_3Bi_2I_9$ films were obtained by using a Rigaku IV X-ray diffractometer using a Cu Kα X-ray source ($\lambda = 1.5405$ Å) within a diffraction angle (2θ) range from 5° to 60°. X-ray photoelectron spectroscopy (XPS) was performed using a PHI Versa Probe II spectrometer (Physical Electronics) with a photon energy of 1486.6 eV (Al Kα). The absorption spectrum of a $MA_3Bi_2I_9$ film deposited onto an ITO substrate was measured using a Perkin-Elmer Lambda 950 spectrometer equipped with a 150 mm integrating sphere, a PMT detector, a tungsten halogen lamp for the visible region (350–800 nm), and a deuterium lamp for the ultraviolet region (250–350 nm). The scan rate for the measurement was 0.4 nm s^{-1}, and the data interval was 1.0 nm. The film was placed in the center of the integrating sphere to collect both the transmitted, T, and the reflected, R, (including the spectrally reflected and diffusely scattered) light with the PMT detector. The transflectance measurement allowed for the absorbance, A, of the film to be determined by $A = -\log(T + R)$. To measure changes in the absorption of the $MA_3Bi_2I_9$ films over time while exposed to ambient conditions, a Shimadzu UV-1800 spectrophotometer was used to measure the optical transmittance of films deposited on glass substrates.

The electrochemical analysis was performed with a standard three-electrode cell using the cyclic voltammetry (CV) mode in a Biologic potentiostat (SP-200, Bio-Logic SAS) with a scan rate of 20 mV s^{-1}. A glassy carbon electrode was used as the working

24730 | *J. Mater. Chem. A*, 2017, **5**, 24728–24739

This journal is © The Royal Society of Chemistry 2017

electrode to measure the formal potential of ferrocene/ferrocenium (Fc/Fc$^+$), whereas a Pt foil acted as the counter electrode. Silver (Ag) wire in 0.01 M AgNO$_3$ + 0.1 M tetrabutylammonium hexafluorophosphate (TBAPF$_6$) (98%, Aldrich) in acetonitrile (99.9%, Sigma-Aldrich) was used as the reference electrode (BAS Inc.). The conduction band (CB) energy was calculated from the onset of reduction potential (E_{red}) values, assuming the energy level of Fc/Fc$^+$ to be −4.8 eV below the vacuum level. The formal potential of Fc/Fc$^+$ was measured to be 0.075 V against a Ag/Ag$^+$ reference electrode in an electrolyte consisting of 0.001 M ferrocene in 15 mL of 0.1 M TBAPF$_6$ in acetonitrile solution. Therefore, from eqn (1)

$$E_{CB}(E_{LUMO}) = -(E_{red} + 4.725) \text{ eV}, \tag{1}$$

where the onset potential values (E_{red}) are relative to the Ag/Ag$^+$ reference electrode. The valence band (VB) energy, $E_{VB}(E_{HOMO})$, was calculated based on the band gap value determined from UV-vis spectra, $E_{VB}(E_{HOMO}) = E_{CB} - E_g(\text{indirect})$. MA$_3Bi_2I_9$ films deposited on glass slides were dissolved in a solution of 0.1 M tetrabutylammonium hexafluorophosphate (TBAPF$_6$) in acetonitrile for conducting these tests.

All electronic transport property measurements were carried out using a commercial probe station (Janis ST500-1-2CX) with Cu–Be probe tips having 50 μm tip diameter. A Keithley 2400 source meter was used for resistivity measurements on MA$_3$Bi$_2$I$_9$ films deposited on 5 mm × 5 mm high-purity quartz substrates. van der Pauw structures were created by first sputtering 50 nm Pt on the four corners of the quartz substrates prior to MA$_3$Bi$_2$I$_9$ deposition. After MA$_3$Bi$_2$I$_9$ deposition, indium dots were attached to these four corners and served as the contact electrodes for the four probe tips. The corresponding Hall measurements were done by placing an Fe–Nd ring magnet around the sample. The magnetic field strength at the center of the ring magnet was 2135 G. The pressure in the chamber was maintained at or below 1 × 10^{-4} Torr.

2.4 DFT calculation details

DFT calculations were performed using the Vienna *Ab initio* Simulation Package (VASP).[33] We employed the Perdew–Burke–Ernzerhof exchange–correlation (XC) functional revised for solids (PBEsol).[34] The core and valence electrons were modeled using the projector-augmented-wave (PAW) method.[35] We used a plane-wave basis set with a cutoff of 500 eV and performed relaxation until the Hellmann–Feynman forces on the atoms were less than 0.001 eV Å^{-1}. The Brillouin zone was sampled using a gamma-centered Monkhorst–Pack[36] k-point mesh while keeping the k-point density ($nk \times a$), where nk is the number of k-points and a is the lattice parameter, which is equal to ∼26 for structural relaxation and ∼52 for electronic structure calculations. The spin–orbit coupling (SOC) effects were included for calculating the electronic band structure and the absorption spectra. The charge partitioning for the Bader charge analysis was carried out using the approach developed by Henkelman *et al.*[37–39] The elemental charges, used for Bader charge analysis, are the difference between the total valence electrons considered in the PAW potential and the total electrons assigned to an

element after the charge density partitioning. The band-edge alignment for MA$_3$Bi$_2$I$_9$ was performed using a surface slab with a material thickness of ∼55 Å and a vacuum of ∼50 Å. The valence band edge (E_{VB}) is calculated using the expression $E_{VB} = \phi_{VAC} - \varepsilon_{VB}$, where ϕ_{VAC} is the vacuum electrostatic potential and ε_{VB} is the eigenvalue for the valence band maxima. The conduction band edge (E_{CB}) is calculated using the expression $E_{CB} = E_{VB} + E_G$, where E_G is the band gap calculated using PBEsol with SOC.

3 Results & discussion

3.1 Materials characterization

Fig. 2a shows the color of the films on glass substrates as a function of deposition time. Initially, for short times (<60 minutes), there is hardly any deposition observed. After 90 minutes of reaction, a visible orange color is seen on the glass substrate. We note that there is a stronger color close to the upstream side of the sample, indicating that the deposition is determined by the Ar flow. For deposition times ≥180 minutes, a continuous film is observed on the glass substrate. The orange color is characteristic of MA$_3$Bi$_2$I$_9$.[15] The successful deposition of MA$_3$Bi$_2$I$_9$ films on Willow® glass – Corning's flexible glass substrates is shown in Fig. 2b and c. These flexible glass substrates can withstand temperatures up to 500 °C and thus can be used for the APCVD of MA$_3$Bi$_2$I$_9$ films.

High-magnification SEM images are shown for the same substrates in Fig. 3. The mechanistic aspects of the deposition process can be garnered from this sequence of images. First, Fig. 3a–c (*i.e.*, for deposition times 15, 30 and 45 minutes) show isolated hexagonal crystals growing in size from 0.5 μm for 15
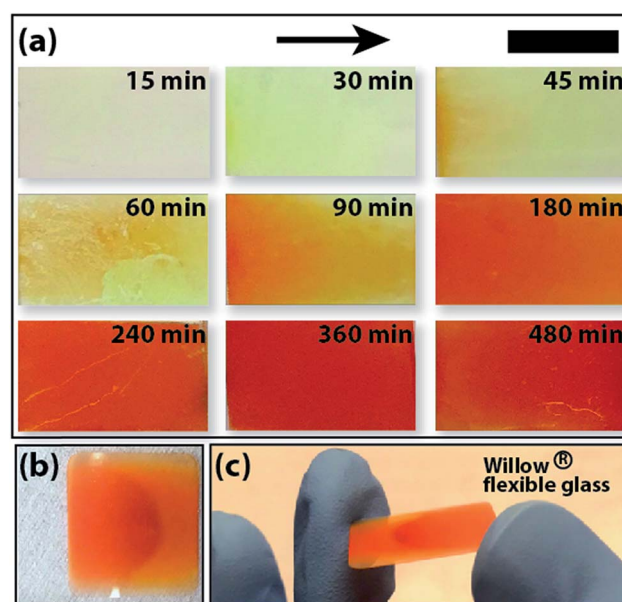
Fig. 2 (a) Optical images of APCVD MA$_3$Bi$_2$I$_9$ films on a glass substrate for varying times of deposition. Arrow represents the direction of the Ar flow in the furnace. Scale bar = 1 cm. (b) MA$_3$Bi$_2$I$_9$ deposited for 360 minutes on Willow® flexible glass of size 2 cm × 2 cm and (c) substrate held in hand.

This journal is © The Royal Society of Chemistry 2017

J. Mater. Chem. A, 2017, **5**, 24728–24739 | **24731**
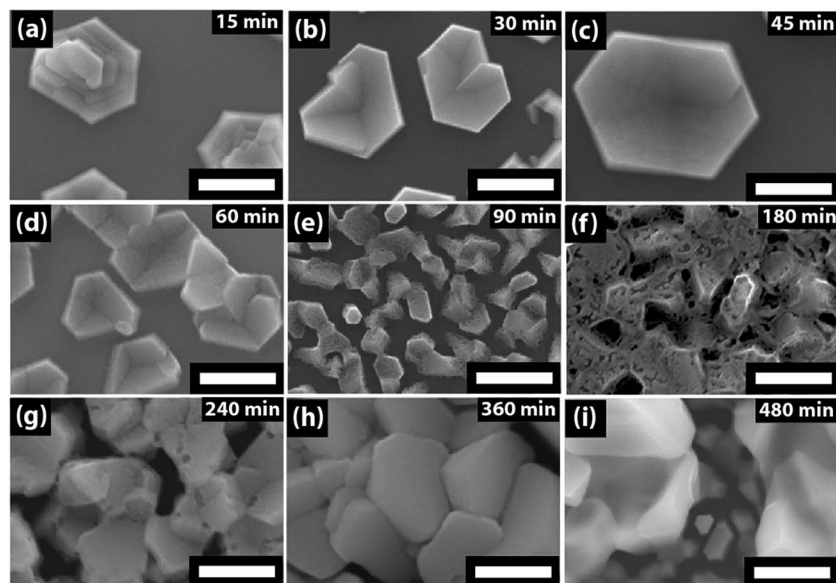
Fig. 3   SEM images of APCVD films for varying times of deposition. Scale bar = 500 nm.

minutes to 1.0 µm for 45 minutes of deposition. The crystal shape is characteristic[40] of BiI_3 and has been independently confirmed through Raman (see ESI S3†) and XRD measurements, as will be shown below. Thus, in the initial part of the deposition scheme, isolated BiI_3 crystals (0.5–1.0 µm in diameter) are deposited on the substrate surface.

The BiI_3 crystals show signs of MAI incorporation starting at 60 minutes (Fig. 3d). While the crystal shapes remain intact, the surface of the crystal shows marked roughness. For 90 minutes (Fig. 3e), the deposited structure becomes interconnected. The interconnected structure shows signs of growth for 180 minutes (Fig. 3f) while the surface structure is rough and full of pinholes.

The surface structure further changes for the 240 minute sample (Fig. 3g), where well-crystallized $MA_3Bi_2I_9$ grains are visible, though evidence of MAI incorporation can still be seen at the grain boundaries. For the 360 minute sample (Fig. 3h), the $MA_3Bi_2I_9$ polycrystalline grains are well developed, indicating the complete incorporation of the MAI. However, there are intergranular gaps observed, and such a morphology is not ideal for thin film photovoltaic applications. Finally, for the 480

minute sample (Fig. 3i), we see secondary nucleation of grains in between larger polycrystalline grains.

The secondary nucleation of the $MA_3Bi_2I_9$ crystals observed in the intergranular regions of the film has been used to grow a dense, compact and polycrystalline film. In Fig. 4a a low-magnification image of the 360 minute sample is shown. The intergranular regions are clearly observed and, as indicated before, are sites for secondary nucleation after 480 minutes of deposition. Therefore, repeating the process (labeled henceforth as 360 minute (2×)) can eliminate these gaps and produce a film with a dense morphology. This is shown in Fig. 4b. While such an approach may take excessively long deposition times, its need is dictated primarily by the limited mass loading of the MAI and BiI_3 precursors in our sublimation crucibles. Larger furnace reactors may easily overcome such hardware limitations and yield dense films in a single process run. The 'twice deposited' films were subsequently used to conduct all optical and electrical measurements.

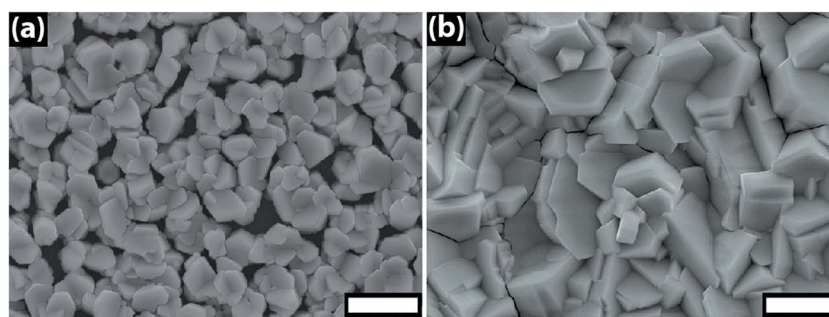The XRD data of $MA_3Bi_2I_9$ samples deposited for times varying from 15 minutes to 60 minutes are shown in Fig. 5a.

Fig. 4   (a) Low magnification image of the $MA_3Bi_2I_9$ film deposited for 360 minutes showing the intergranular gaps in the polycrystalline film. (b) A repeat of the same process (i.e., 360 minutes (2×)) eliminates these gaps and produces a dense, polycrystalline film. All optical and electrical measurements were performed on the 360 minute (2×) sample. Scale bar = 2 µm.
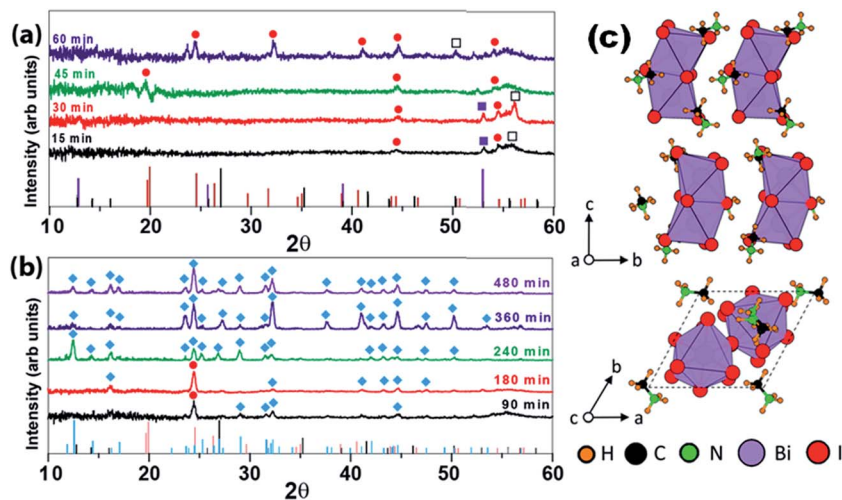
Fig. 5 XRD of films as a function of deposition time. For clarity, the XRD has been split into two graphs. (a) Variation of deposition time from 15 minutes to 60 minutes and (b) variation of deposition time from 90 minutes to 480 minutes. Single crystal BiI_3 reference is obtained from Boopathy et al., and is indexed to the symbol '■' with violet staffs. Polycrystalline BiI_3 is indexed to the symbol '□' and black staffs and obtained from JCPDS 48-1795. MAI reference is obtained from JCPDS 10-0737 and is indexed to the symbol '●' and red staffs. $MA_3Bi_2I_9$ reference is obtained from Abulikemu et al., and is indexed to the symbol '◆' and cyan staffs. (c) Crystal structure of $MA_3Bi_2I_9$ after relaxation along (100) (top) and (001) (bottom) crystallographic directions.

Initially a diffraction peak corresponding to single crystal BiI_3 with the violet symbol '■' can be seen. The peak at $2\theta = 52.9°$ can be indexed[41] to BiI_3 (0012). The other peaks represent MAI, marked by the red symbol '●' (JCPDS ref no. 000-10-0737) at 54.6° corresponding to (222), and a slightly displaced peak from polycrystalline BiI_3 (JCPDS 48-1795) given as '□' at 56.2° corresponding to (226). As the deposition time increases, it can be seen that the presence of MAI (JCPDS 10-0737) becomes prominent and the single crystal and polycrystalline BiI_3 signals diminish.

Fig. 5b shows the XRD for deposition times varying from 90 minutes to 480 minutes. After 90 minutes of deposition, the presence of $MA_3Bi_2I_9$ is detectable. The $MA_3Bi_2I_9$ phase is denoted by the cyan '◆' symbol. Here, we note that there are no JCPDS files available for $MA_3Bi_2I_9$, and we use the patterns generated by Abulikemu et al.,[42] to index our peaks. Initially at 90 minutes, peaks at 29.07° (024), 31.6° (025), 32.38° (116) and 44.7° (029) are observed. A strong peak at 24.6° corresponds to MAI (110). Though unlikely at this early stage of deposition, this peak could also represent the $MA_3Bi_2I_9$ (006) peak at 24.5°. At 180 minutes, the primary peak is still assigned to MAI (110) at 24.6°. Beyond 180 minutes, multiple peaks of $MA_3Bi_2I_9$ start to emerge. The peak at 24.6° can now be assigned to $MA_3Bi_2I_9$ (006), given that there are associated peaks, all corresponding to the emerged $MA_3Bi_2I_9$ phase. Other strong peaks corresponding to $MA_3Bi_2I_9$ observed are at 23.6° (015), 25.3° (022), 32.2° (116), 41.07° (028), 44.7° (029) and 50.1° (136). The characteristically polycrystalline nature of the $MA_3Bi_2I_9$ films is in-line with the SEM data since polycrystallinity is clearly shown in the SEM images for 240, 360 and 480 minute samples. Finally, we note that there appears to be a weak peak observed for the 240 minute sample at 35.2° corresponding to the (116) plane in polycrystalline BiI_3 which could indicate the concurrent

deposition of BiI_3 during $MA_3Bi_2I_9$ formation, but this peak is not detected for the 360 and 480 minute samples.

Next, we compare the lattice parameters from our XRD results to the crystal structure data obtained from first-principles DFT calculations. $MA_3Bi_2I_9$ exhibits a hexagonal crystal symmetry at room temperature with the $P63/mmc$ space group.[43–45] The methylammonium cation ($CH_3NH_3^+$ (MA^+)) shows no preferential ordering in the hexagonal phase.[43] Fig. 5c shows the DFT-optimized crystal structure of $MA_3Bi_2I_9$ oriented along [100] and [001] directions. The geometry optimization has been performed using the PBEsol functional,[34] which gives good agreement of theoretical lattice parameters with the experimental values. The calculated lattice parameters from DFT are 8.72 Å, 8.27 Å and 21.76 Å, which are, respectively, within 1.77%, 3.47% and 0.01% of the experimental[43] lattice parameters of the hexagonal phase. Since, we use a static ground-state orientation of the MA cation in our DFT calculations, the ideal hexagonal $P63/mmc$ symmetry of the lattice is broken, which results in lowering of the symmetry for the relaxed structure. Instead the DFT relaxed structure exhibits a monoclinic symmetry with the space group Cc, which is a subgroup of $P63/mmc$.

The $MA_3Bi_2I_9$ structure can be thought of as a derivative of the perovskite (ABX_3) structure. In both cases the B-site cation (Bi in the case of $MA_3Bi_2I_9$) is octahedrally coordinated by X-site anions (I in the case of $MA_3Bi_2I_9$). However, as compared to the ideal perovskite structure, only $2/3^{rd}$ of the total octahedral sites are occupied by the Bi cation in $A_3Bi_2I_9$ compounds.[16] Additionally, as opposed to the corner-connected octahedral network of BX_6 octahedra in perovskites, $MA_3Bi_2I_9$ forms a layered structure consisting of isolated $Bi_2I_9^{3-}$ bioctahedra. These bioctahedra are formed by two face-shared BiI_6 octahedra, which share three I anions (Fig. 5c).

This journal is © The Royal Society of Chemistry 2017
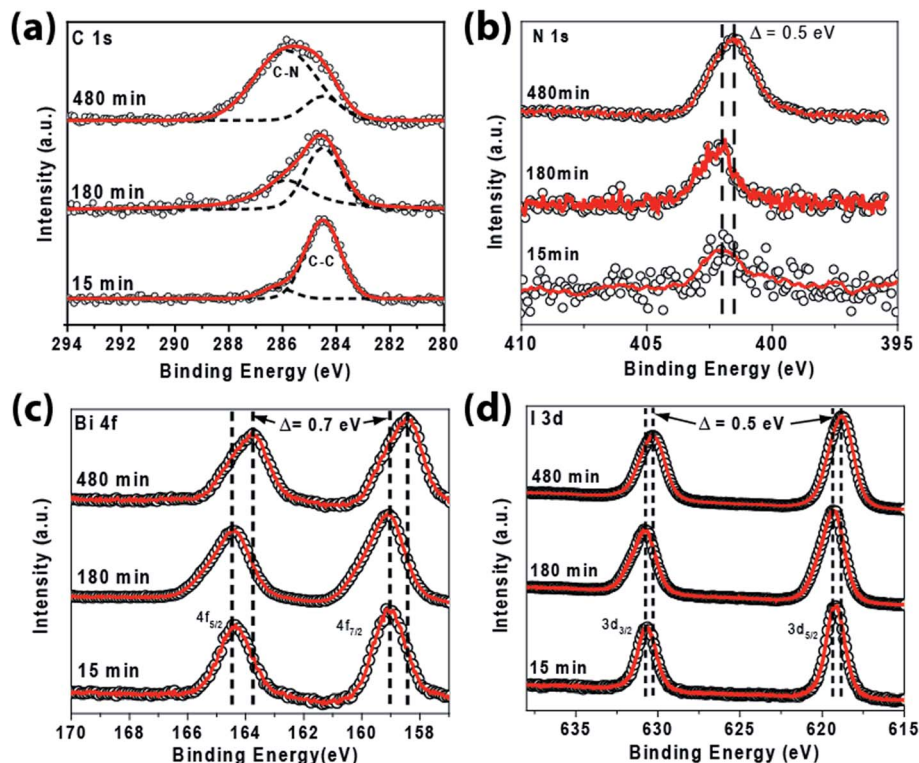
J. Mater. Chem. A, 2017, 5, 24728–24739 | 24733

Fig. 6 XPS fine spectra obtained from 15, 180 and 480 minute $MA_3Bi_2I_9$ thin films showing (a) C 1s, (b) N 1s, (c) Bi 4f and, (d) I 3d. The carbon 1s peak has been deconvoluted into two peaks related to adventitious carbon (284.5 eV) and C–N from the methylammonium group.

Fig. 6 shows the XPS fine spectra of the 15, 180 and 480 minute $MA_3Bi_2I_9$ films whereas the full survey spectra of these samples are provided in ESI S4.† In Fig. 6a, the C 1s fine spectrum is shown. For the 15 minute sample, the primary peak is at 284.5 eV corresponding to the C–C bond related to adventitious carbon. There is a slight shoulder detected at 282.6 eV, which is related to the C–N bond[46] originating from MAI. The C–N bond increases in strength for the 180 minute sample and dominates the C 1s signal for the 480 minute sample. These data suggest that MAI incorporation in the BiI_3 is a slower process than the BiI_3 condensation, nucleation and growth process. This conclusion is in line with earlier observations made from the vapor pressure calculations in Table 1 as well as the SEM images in Fig. 3.

N 1s, Bi 4f and I 3d XPS fine spectra are provided in Fig. 6b–d, respectively, and the peak positions are shown in Table 2. For the N 1s, the 15 minute sample shows a weak signal but the signal progressively grows stronger for the 180- and 480 minute

samples indicating MA^+ incorporation. The N 1s peak position shifts to a lower binding energy from 402.0 eV to 401.5 eV. The Bi 4f and I 3d peaks are strong even at 15 minutes and indicate the presence of BiI_3. MA^+ incorporation produces a shift to a lower binding energy of 0.7 eV and 0.5 eV in the Bi 4f and I 3d peaks, respectively. The peak-shifts indicate electron transfer to the N, Bi and I during the transformation of BiI_3 to $MA_3Bi_2I_9$.

To explain the shifts in the XPS spectra, Bader charge analysis has been performed for each element during the chemical reaction leading up to the formation of $MA_3Bi_2I_9$. The average Bader charges for each elemental species in $MA_3Bi_2I_9$, MAI and BiI_3 are shown in Table 3. Recall that in Fig. 6a, the intensity of the de-convoluted C–N peak increases as the reaction proceeds, indicating an increased presence of C–N bonds with increasing reaction time. The C–N bonding occurs at a higher binding

Table 2 XPS peak positions of N 1s, Bi $4f_{7/2}$ and I $3d_{5/2}$ in the $MA_3Bi_2I_9$ films deposited for 15, 180 and 480 minutes

Sample	Binding energy (eV)		
	N 1s	Bi $4f_{7/2}$	I $3d_{5/2}$
15 min	402.0	159.1	619.3
180 min	402.0	159.0	619.2
480 min	401.5	158.4	618.8

Table 3 Calculated average Bader charges and their respective standard deviation (in the units of e) for each elemental species in $MA_3Bi_2I_9$, MAI and BiI_3

Element	$MA_3Bi_2I_9$	MAI	BiI_3
C	0.453 ± 0.015	0.445	
N	-2.982 ± 0.009	-3.029	
Bi	1.049 ± 0.002		1.061
I	-0.472 ± 0.009	-0.668	-0.354
H-1 (bonded to C)	0.081 ± 0.013	0.084 ± 0.005	
H-2 (bonded to N)	1	1	

energy compared to the C–C bonding, signifying the loss of electrons in the C atom upon N addition. From the Bader analysis, one finds the loss of electrons in the C atom confirmed by the higher atomic charge on C in $MA_3Bi_2I_9$ $(+0.453 \pm 0.015)e$ than in MAI $(+0.445e)$. However, for N there is disagreement between the calculated charge transfer and the shift in the XPS peak presented in Fig. 6b. According to the calculated Bader charges, the average charge on N is $(-2.982 \pm 0.009)e$ and $(-3.029e)$ for $MA_3Bi_2I_9$ and MAI respectively, which means that the N anion is being oxidized while going from MAI to $MA_3Bi_2I_9$. However, this charge transfer is not supported by the shift in the XPS peak towards a lower binding energy with increasing reaction time, which points towards the reduction (gain in electrons) of the N anion. This disagreement could be attributed to the weak XPS intensity for N at reaction times of 15 and 180 minutes, which makes the determination of charge transfer difficult with the N 1s fine spectra.

The Bi cations in $MA_3Bi_2I_9$ have an average charge of $(+1.049 \pm 0.002)e$ compared to $+1.061e$ in the reactant BiI_3 and are, therefore, in a reduced state in $MA_3Bi_2I_9$ as compared to BiI_3. This reduction of the Bi cation is also supported by the shift in the experimental XPS peak towards a lower binding energy as shown in Fig. 6c. On comparing the average Bader charge of I anions in the primary reactants, *i.e.* the weighted average of the Bader charge of I in MAI and BiI_3 $(-0.459e)$ to that in $MA_3Bi_2I_9$ $(-0.472e)$, we find that the I anions are also reduced. This gain of electrons is also confirmed by the shift of the XPS peak for the I anion towards a lower binding energy as shown in Fig. 6d. Moreover, the reduction of Bi and I ions in $MA_3Bi_2I_9$ with respect to the reactants (MAI and BiI_3) is accompanied by a simultaneous

oxidation of the MA cations in $MA_3Bi_2I_9$ with respect to MAI, which balances out the net charge transfer. The net reduction of Bi and I requires a total charge transfer of $0.141e$ per formula unit of $MA_3Bi_2I_9$ to Bi and I ($0.024e$ for Bi and $0.117e$ for I). This charge transfer is achieved by a transfer of electrons from MA cations to Bi and I as the reaction proceeds. The net average charge on MA cations is $(+0.668e)$ and $(+0.715e)$ in MAI and $MA_3Bi_2I_9$ respectively, which amounts to a net charge transfer of $0.141e$ per formula unit of $MA_3Bi_2I_9$ from MA to Bi and I.

Finally, the charge transfer in H can be categorized into two types, based on the position of H in the MA cations. H atoms directly bonded to C and those directly bonded to N lead to two different bonding environments. The H atoms bonded to N show an atomic charge of +1 for both $MA_3Bi_2I_9$ and MAI, whereas the H atoms bonded to C show an average atomic charge of +0.081 and +0.084 in $MA_3Bi_2I_9$ and MAI, respectively. This difference in the atomic charge is due to the higher electronegativity of N than C, which makes the H–N bonds more ionic than the H–C bonds.

3.2 Optical characterization

Fig. 7a shows the UV-vis absorption spectra of the 360 minute (2×) $MA_3Bi_2I_9$ film at wavelengths between 400 nm and 800 nm. The absorption onset of $MA_3Bi_2I_9$ was observed at approximately 600 nm. The presence of a peak at 511 nm before the onset of continuous absorption is attributed to excitons.[42,44,47,48] We have verified separately that the MAI and BiI_3 absorption spectra do not contain an exciton peak. This exciton peak has also been observed for single crystals of $MA_3Bi_2I_9$ at temperatures between 78 K and 301 K, and it starts to broaden as the

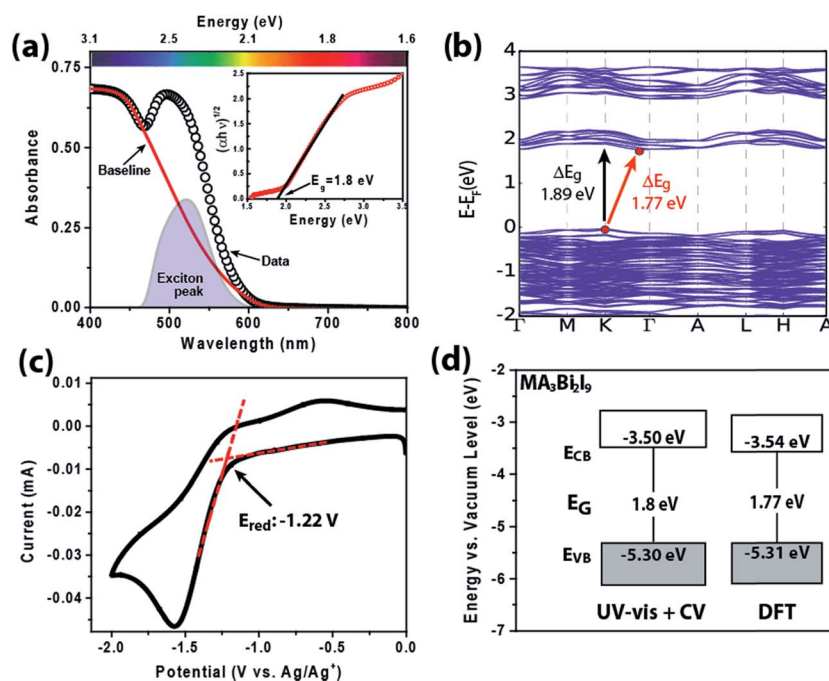**Fig. 7** (a) UV-vis spectra of the $MA_3Bi_2I_9$ film. Exciton peak is extracted and a Tauć plot of the baseline is used to measure the indirect bandgap of 1.8 eV. (b) DFT-calculated band structure for $MA_3Bi_2I_9$ with a calculated indirect bandgap of 1.77 eV (red arrow) and direct bandgap of 1.89 eV (black arrow). (c) Cyclic voltammetry curve (*vs.* Ag/Ag⁺ electrode) for $MA_3Bi_2I_9$. (d) Band edge information from experiment (UV-vis + CV) and DFT calculations.

Table 4 Comparison of Hall measurement data of $MA_3Bi_2I_9$ films deposited using various synthesis techniques

Synthesis process	Thickness (nm)	Conductivity (S cm^{-1})	Mobility (cm^2 V^{-1} s^{-1})	Carrier density (cm^{-3})
APCVD, 360 minutes (2×), (this work)	775	9.7	18.0	n-type, 3.36×10^{18}
Solution processed, (Lyu et al.,[20])	500	0.0083	1.0	p-type, 10^{16}
Solution processed, sulphur doped, (Vigneshwaran et al.,[53])	Unknown	839	2.28	p-type, 2.3×10^{21}

temperature increases.[47] The thickness dependence of the exciton levels is shown in ESI S5† where a stronger and narrower exciton peak is observed for a thinner film (~480 nm), whereas a broader exciton peak is observed for a thicker (~1000 nm) film.

The bandgap of $MA_3Bi_2I_9$ films was calculated first by establishing a baseline and removing the exciton peak from the absorption spectrum and then by plotting the baseline as a Tauć plot and using the equation[49]

$$\alpha h\nu = \beta(h\nu - E_g)^n \qquad (2)$$

where α is the absorption coefficient, $h\nu$ is the photon energy, β is a constant, and E_g is the bandgap; a linear fit is used to extract the bandgap. Assuming that the lowest energy optical transition in $MA_3Bi_2I_9$ is indirect (see DFT calculations below), $n = 2$ is used in the evaluation. The inset of Fig. 7a shows the Tauć plot, and the extrapolated bandgap is 1.80 eV. The value of the $MA_3Bi_2I_9$ bandgap is in line with those reported by Lyu et al.[20]

Fig. 7b shows the electronic band structure of $MA_3Bi_2I_9$ calculated using PBEsol with spin–orbit coupling (SOC) along the high symmetry points in the Brillouin zone. Using the PBEsol functional and SOC effects, we find that $MA_3Bi_2I_9$ has an indirect band gap of 1.77 eV from K (1/3, 1/3, 0) in the valence band to (0.05, 0.05, 0) in the conduction band as shown in Fig. 7b. The calculated direct band gap is 1.89 eV and occurs at (0.075, 0.075, 0). The indirect and direct transitions are shown as red and black arrows respectively in Fig. 7b. $MA_3Bi_2I_9$ exhibits relatively flat bands as compared to more promising organohalide perovskite solar cell absorbers such as $CH_3NH_3PbI_3$,[50,51] which is typical of $A_3Bi_2I_9$ compounds[17] because of the disrupted octahedral-connectivity along all three crystallographic directions.

We also calculated the band structure using the hybrid Heyd–Scuseria–Ernzerhof (HSE06) functional with SOC effects,[52] which is known to result in better band gap estimation for a variety of semiconductors, as shown in ESI S6.† We find that HSE06 overestimates the bandgap with an indirect band gap of 2.41 eV from K (1/3, 1/3, 0) in the valence band to (0.05, 0.05, 0) in the conduction band, and a direct band gap of 2.53 eV at K (1/3, 1/3, 0). Both the indirect and direct transitions are shown as red and black arrows respectively in Fig. S6.†

To extract the experimental band edge positions of $MA_3Bi_2I_9$, CV measurements are shown in Fig. 7c. $MA_3Bi_2I_9$ has the reduction peak edge at $E_{red} = -1.22$ V. Referring to eqn (1), the $MA_3Bi_2I_9$ conduction band edge position is therefore calculated to be $E_{CB} = -3.505$ eV with respect to vacuum. Using the bandgap obtained from UV-vis (1.80 eV), the valence band edge position is

calculated to be $E_{VB} = -5.30$ eV. The data from UV-vis + CV measurements and DFT calculations are summarized in Fig. 7d.

3.3 Electrical characterization

For the $MA_3Bi_2I_9$ film deposited twice (360 minute (2×)) on the quartz substrate, conductivity was measured using a van der Pauw four-point configuration. The conductivity is 9.7 S cm^{-1} (i.e., resistivity 0.103 Ω cm) at room temperature for a film with a thickness of 775 nm (see ESI S7† for thickness measurement using the cross-sectional SEM image). The detailed result is shown in Table 4 along with the comparison of electrical data from other reports.[15,44] This conductivity is 1168× better than the reported conductivity (0.0083 S cm^{-1}) of a solution-processed,[20] 500 nm $MA_3Bi_2I_9$ film highlighting the importance of the type of synthesis in determining film properties.

Room temperature Hall measurements were performed to determine the conductivity type, carrier mobility and concentration of the $MA_3Bi_2I_9$ film. According to the measurements, the Hall coefficient is negative, which indicates the carriers to be n-type for the CVD $MA_3Bi_2I_9$ film. This result is in contrast to the solution processed $MA_3Bi_2I_9$ film which shows p-type conductivity.[20,53] Furthermore, the calculated carrier concentration of the CVD $MA_3Bi_2I_9$ film is 3.36×10^{18} cm^{-3}, which is 2 orders higher in magnitude than that of solution-based, undoped $MA_3Bi_2I_9$ films.[20,53] Finally, the mobility was estimated to be 18 cm^2 V^{-1} s^{-1}. This is higher compared to the mobility reported by Lyu et al.,[20] i.e., 1 cm^2 V^{-1} s^{-1}, and Vigneshwaran et al.,[53] i.e., 2.28 cm^2 V^{-1} s^{-1}. The improved carrier concentration and mobility highlight typical advantages that vapor phase processing of $MA_3Bi_2I_9$ films have over solution-based techniques including minimal impurities and better crystallinity and film morphology.

3.4 Film stability

It has been reported that $MA_3Bi_2I_9$ is stable under ambient conditions, thus presenting a significant advantage over other organic halide perovskite candidates.[54] However, in our work we find that the $MA_3Bi_2I_9$ film exposed to ambient conditions (room temperature, 45% humidity and 1 atm) undergoes changes in its composition and degradation in its optical and electrical properties. In Fig. 8a, a loss of N is detected in the $MA_3Bi_2I_9$ film exposed to ambient conditions in just 5 days. The absence of N has been observed by Li et al.,[55] for degraded Pb-based perovskite films as well. Furthermore, in ESI S8,† we provide the XPS 1s fine spectra of O and 4f of Bi in the $MA_3Bi_2I_9$ film. The O 1s shows the characteristic O peak associated with surface adsorbed hydroxyl groups with an additional shoulder corresponding to Bi–O bond formation after 5 days and growing
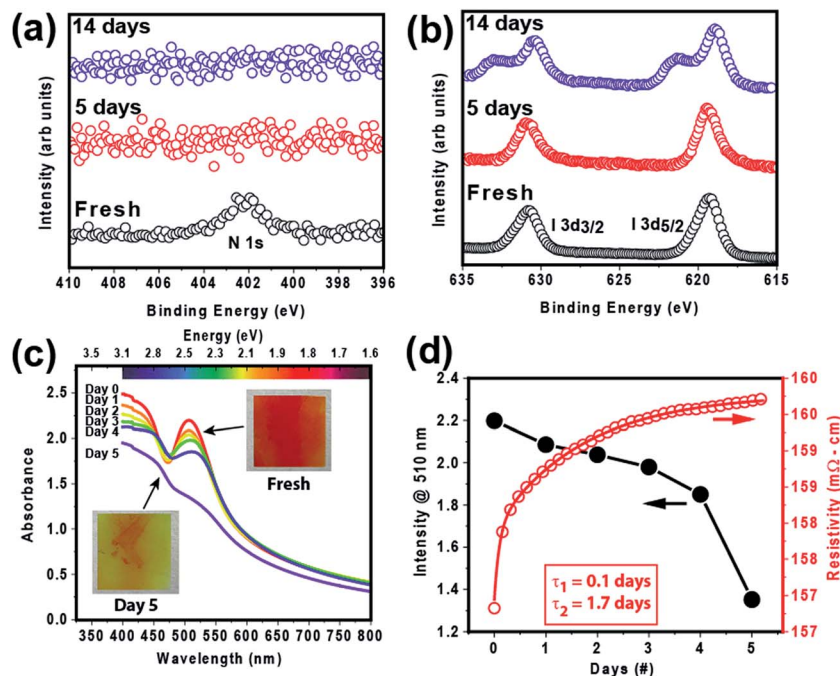
24736 | J. Mater. Chem. A, 2017, 5, 24728–24739

This journal is © The Royal Society of Chemistry 2017

Fig. 8 (a) XPS fine spectra of N 1s show the absence of N after just 5 days exposure to ambient conditions. (b) XPS fine spectra of I 3d for fresh and after 5 (no change) and 14 days under ambient conditions. The splitting of the 3d peaks after 14 days at higher binding energy indicates the oxidation of the iodine. (c) UV-vis spectra from day 0 (fresh) to day 5 show a gradual decay of the excitonic peak while insets show the actual film color fading, and (d) change in the exciton peak intensity (black, left axis) and electrical resistivity (red, right axis) as a function of number of days exposed to ambient conditions. The increase in resistivity follows a bi-exponential decay with time constants 0.1 and 1.7 days.

stronger after 14 days of exposure to ambient conditions. Similarly, the Bi 4f shows signs of oxidation as well after 5 days. Fig. 8b shows XPS fine spectra of I $3d_{7/2}$ and $3d_{5/2}$ for fresh films and for films exposed for 5 and 14 days to ambient conditions. Unlike N and O, there is no noticeable change observed in the I 3d fine spectra after 5 days. However, shoulders appear for the I $3d_{7/2}$ and $3d_{5/2}$ peaks on the higher binding energy side after 14 days, indicating the oxidation[56] of I. Thus, from the XPS data it can be concluded that, while the loss of surface N and oxygen incorporation (most likely associated with Bi) is a rapid process, iodine oxidation is a slower process.

The compositional changes in $MA_3Bi_2I_9$ are accompanied by changes in optical and electrical properties. Fig. 8c shows the UV-vis absorption spectra of the $MA_3Bi_2I_9$ film exposed to ambient conditions over a period of 5 days. The characteristic 511 nm exciton peak disappears on day 5. Correspondingly, the insets in Fig. 8c show the film color changes from bright orange to a pale shade of yellow. In Fig. 8d, the excitonic intensity at 511 nm (black, left axis) and the 4-wire resistivity (red, right axis) are plotted as a function of time over a five day period. A bi-exponential model involving two time constants is used to fit the increase in resistivity over time. Two time constants, $\tau_1 = 0.1$ day and $\tau_2 = 1.7$ days, are obtained with a model fit that has an adjusted $r^2 \sim 0.99$.

The XPS analysis along with the bi-exponential decay of resistance suggests that two decay mechanisms might be operative in the degradation of the $MA_3Bi_2I_9$ films. First, the time constant $\tau_1 = 0.1$ day could indicate the surface oxidation of $MA_3Bi_2I_9$ where the Bi may be oxidized to Bi_2O_3. In line with this

assumption, it can be seen that the exciton peak intensity only slightly degrades in the initial period. This is because the surface Bi_2O_3 layer may provide temporary protection[24] from further attack by ambient O_2, keeping the excitonic modes active in the bulk. On the other hand $\tau_2 = 1.7$ days indicates the slower diffusion-limited oxidation of the bulk $MA_3Bi_2I_9$, and as the film gets oxidized after day 4, the exciton peak intensity rapidly degrades.

4 Conclusions

In conclusion, we have demonstrated an atmospheric pressure chemical vapor deposition process for the deposition of a $MA_3Bi_2I_9$ film. The film is deposited using co-sublimation of methylammonium iodide (kept at 199 °C) and BiI_3 (kept at 230 °C) as precursors in a flow of inert argon. The temperature of deposition is 160 °C. The key advantage of this synthesis approach is that the deposition is at atmospheric pressure and at low temperatures, which opens the possibility for depositing $MA_3Bi_2I_9$ films in high volume, cleanroom compatible, manufacturing environments. The deposition on flexible Willow® glass has been demonstrated.

Well-developed crystals are obtained after 360 minutes of deposition. Repeating the process twice leads to dense, high quality polycrystalline films. The optical bandgap is measured to be 1.80 eV. Room temperature Hall measurements on 775 nm thick $MA_3Bi_2I_9$ films indicate them to be n-type with a carrier concentration of 3.36×10^{18} cm^{-3} and a Hall mobility of 18 cm^2 V^{-1} s^{-1}, which are superior to those of solution processed, undoped films.

This journal is © The Royal Society of Chemistry 2017

J. Mater. Chem. A, 2017, **5**, 24728–24739 | **24737**

The $MA_3Bi_2I_9$ films oxidize under ambient conditions in a matter of ~5 days and in the process, (1) N is lost, (2) excitonic peaks are quenched, and (3) resistivity increases with a bi-exponential decay with time constants related to a fast surface oxidation mechanism, followed by a slower oxidation of the bulk film.

Conflicts of interest

There are no conflicts to declare.

Acknowledgements

References

1 A. Kojima, K. Teshima, Y. Shirai and T. Miyasaka, *J. Am. Chem. Soc.*, 2009, **131**, 6050–6051.

2 NREL, Best Research-Cell Efficiencies, https://www.nrel.gov/pv/assets/images/efficiency-chart.png.

3 C. Wehrenfennig, G. E. Eperon, M. B. Johnston, H. J. Snaith and L. M. Herz, *Adv. Mater.*, 2014, **26**, 1584–1589.

4 J.-H. Im, C.-R. Lee, J.-W. Lee, S.-W. Park and N.-G. Park, *Nanoscale*, 2011, **3**, 4088–4093.

5 J. H. Noh, S. H. Im, J. H. Heo, T. N. Mandal and S. I. Seok, *Nano Lett.*, 2013, **13**, 1764–1769.

6 S. D. Stranks, G. E. Eperon, G. Grancini, C. Menelaou, M. J. Alcocer, T. Leijtens, L. M. Herz, A. Petrozza and H. J. Snaith, *Science*, 2013, **342**, 341–344.

7 G. Xing, N. Mathews, S. Sun, S. S. Lim, Y. M. Lam, M. Grätzel, S. Mhaisalkar and T. C. Sum, *Science*, 2013, **342**, 344–347.

8 S. F. Hoefler, G. Trimmel and T. Rath, *Monatsh. Chem.*, 2017, **148**, 795–826.

9 B. Hailegnaw, S. Kirmayer, E. Edri, G. Hodes and D. Cahen, *J. Phys. Chem. Lett.*, 2015, **6**, 1543–1547.

10 G. Nagabhushana, R. Shivaramaiah and A. Navrotsky, *Proc. Natl. Acad. Sci. U. S. A.*, 2016, **113**, 7717–7721.

11 A. Babayigit, A. Ethirajan, M. Muller and B. Conings, *Nat. Mater.*, 2016, **15**, 247–251.

12 M. Saliba, T. Matsui, J.-Y. Seo, K. Domanski, J.-P. Correa-Baena, M. K. Nazeeruddin, S. M. Zakeeruddin, W. Tress, A. Abate and A. Hagfeldt, *Energy Environ. Sci.*, 2016, **9**, 1989–1997.

13 Y. Zhou, Z. Zhou, M. Chen, Y. Zong, J. Huang, S. Pang and N. P. Padture, *J. Mater. Chem. A*, 2016, **4**, 17623–17635.

14 N. Rajamanickam, S. Kumari, V. K. Vendra, B. W. Lavery, J. Spurgeon, T. Druffel and M. K. Sunkara, *Nanotechnology*, 2016, **27**, 235404.

15 B. W. Park, B. Philippe, X. Zhang, H. Rensmo, G. Boschloo and E. M. Johansson, *Adv. Mater.*, 2015, **27**, 6806–6813.

16 A. J. Lehner, D. H. Fabini, H. A. Evans, C.-A. Hébert, S. R. Smock, J. Hu, H. Wang, J. W. Zwanziger, M. L. Chabinyc and R. Seshadri, *Chem. Mater.*, 2015, **27**, 7137–7148.

17 X. Huang, S. Huang, P. Biswas and R. Mishra, *J. Phys. Chem. C*, 2016, **120**, 28924–28932.

18 A. Kulkarni, T. Singh, M. Ikegami and T. Miyasaka, *RSC Adv.*, 2017, **7**, 9456–9460.

19 C. T. Zuo and L. M. Ding, *Angew. Chem., Int. Ed.*, 2017, **56**, 6528–6532.

20 M. Lyu, J.-H. Yun, M. Cai, Y. Jiao, P. V. Bernhardt, M. Zhang, Q. Wang, A. Du, H. Wang, G. Liu and L. Wang, *Nano Res.*, 2016, **9**, 692–702.

21 A. M. Ganose, C. N. Savory and D. O. Scanlon, *Chem. Commun.*, 2016, **53**, 20–44.

22 R. E. Brandt, V. Stevanović, D. S. Ginley and T. Buonassisi, *MRS Commun.*, 2015, **5**, 265–275.

23 K. Eckhardt, V. Bon, J. Getzschmann, J. Grothe, F. M. Wisser and S. Kaskel, *Chem. Commun.*, 2016, **52**, 3058–3060.

24 R. L. Hoye, R. E. Brandt, A. Osherov, V. Stevanović, S. D. Stranks, M. W. Wilson, H. Kim, A. J. Akey, J. D. Perkins and R. C. Kurchin, *Chem.–Eur. J.*, 2016, **22**, 2605–2610.

25 T. Okano and Y. Suzuki, *Mater. Lett.*, 2017, **191**, 77–79.

26 Z. Xiao, W. Meng, J. Wang, D. B. Mitzi and Y. Yan, *Mater. Horiz.*, 2017, **4**, 206–216.

27 M. Liu, M. B. Johnston and H. J. Snaith, *Nature*, 2013, **501**, 395–398.

28 Y. X. Zhao and K. Zhu, *J. Phys. Chem. Lett.*, 2014, **5**, 4175–4186.

29 M. M. Tavakoli, L. L. Gu, Y. Gao, C. Reckmeier, J. He, A. L. Rogach, Y. Yao and Z. Y. Fan, *Sci. Rep.*, 2015, **5**, 14083.

30 A. Cuña, I. Aguiar, A. Gancharov, M. Pérez and L. Fornaro, *Cryst. Res. Technol.*, 2004, **39**, 899–905.

31 A. Dualeh, P. Gao, S. I. Seok, M. K. Nazeeruddin and M. Grätzel, *Chem. Mater.*, 2014, **26**, 6160–6164.

32 D. V. Ragone, *Thermodynamics of Materials-I*, Wiley, New York, 1995.

24738 | *J. Mater. Chem. A*, 2017, **5**, 24728–24739

This journal is © The Royal Society of Chemistry 2017

33 G. Kresse and J. Furthmuller, *Phys. Rev. B*, 1996, **54**, 11169–11186.

34 J. P. Perdew, A. Ruzsinszky, G. I. Csonka, O. A. Vydrov, G. E. Scuseria, L. A. Constantin, X. Zhou and K. Burke, *Phys. Rev. Lett.*, 2008, **100**, 136406.

35 P. E. Blöchl, *Phys. Rev. B: Condens. Matter Mater. Phys.*, 1994, **50**, 17953.

36 H. J. Monkhorst and J. D. Pack, *Phys. Rev. B: Solid State*, 1976, **13**, 5188–5192.

37 G. Henkelman, A. Arnaldsson and H. Jónsson, *Comput. Mater. Sci.*, 2006, **36**, 354–360.

38 E. Sanville, S. D. Kenny, R. Smith and G. Henkelman, *J. Comput. Chem.*, 2007, **28**, 899–908.

39 W. Tang, E. Sanville and G. Henkelman, *J. Phys.: Condens. Matter*, 2009, **21**, 084204.

40 D. Nason and L. Keller, *J. Cryst. Growth*, 1995, **156**, 221–226.

41 K. M. Boopathi, S. Raman, R. Mohanraman, F.-C. Chou, Y.-Y. Chen, C.-H. Lee, F.-C. Chang and C.-W. Chu, *Sol. Energy Mater. Sol. Cells*, 2014, **121**, 35–41.

42 M. Abulikemu, S. Ould-Chikh, X. Miao, E. Alarousu, B. Murali, G. O. N. Ndjawa, J. Barbé, A. El Labban, A. Amassian and S. Del Gobbo, *J. Mater. Chem. A*, 2016, **4**, 12504–12515.

43 M. E. Kamminga, A. Stroppa, S. Picozzi, M. Chislov, I. A. Zvereva, J. Baas, A. Meetsma, G. R. Blake and T. T. Palstra, *Inorg. Chem.*, 2017, **56**, 33–41.

44 M. Scholz, O. Flender, K. Oum and T. Lenzer, *J. Phys. Chem. C*, 2017, **121**, 12110–12116.

45 C. Ran, Z. Wu, J. Xi, F. Yuan, H. Dong, T. Lei, X. He and X. Hou, *J. Phys. Chem. Lett.*, 2017, **8**, 394–400.

46 L. Liu, J. A. McLeod, R. Wang, P. Shen and S. Duhm, *Appl. Phys. Lett.*, 2015, **107**, 061904.

47 T. Kawai, A. Ishii, T. Kitamura, S. Shimanuki, M. Iwata and Y. Ishibashi, *J. Phys. Soc. Jpn.*, 1996, **65**, 1464–1468.

48 S. Öz, J.-C. Hebig, E. Jung, T. Singh, A. Lepcha, S. Olthof, F. Jan, Y. Gao, R. German, P. H. M. van Loosdrecht, K. Meerholz, T. Kirchartz and S. Mathur, *Sol. Energy Mater. Sol. Cells*, 2016, **158**, 195–201.

49 J. I. Pankove, *Optical Processes in Semiconductors*, Courier Corporation, 2012.

50 P. Umari, E. Mosconi and F. De Angelis, *Sci. Rep.*, 2014, **4**, 4467.

51 A. S. Thind, X. Huang, J. Sun and R. Mishra, *Chem. Mater.*, 2017, **29**, 6003–6011.

52 J. Heyd, G. E. Scuseria and M. Ernzerhof, *J. Chem. Phys.*, 2003, **118**, 8207–8215.

53 M. Vigneshwaran, T. Ohta, S. Iikubo, G. Kapil, T. S. Ripolles, Y. Ogomi, T. Ma, S. S. Pandey, Q. Shen and T. Toyoda, *Chem. Mater.*, 2016, **28**, 6436–6440.

54 R. L. Hoye, R. E. Brandt, A. Osherov, V. Stevanović, S. D. Stranks, M. W. Wilson, H. Kim, A. J. Akey, J. D. Perkins and R. C. Kurchin, *Chem.–Eur. J.*, 2016, **22**, 1–7.

55 Y. Li, X. Xu, C. Wang, C. Wang, F. Xie, J. Yang and Y. Gao, *J. Phys. Chem. C*, 2015, **119**, 23996–24002.

56 J. Chastain, R. C. King and J. Moulder, *Handbook of X-ray Photoelectron Spectroscopy: a Reference Book of Standard Spectra for Identification and Interpretation of XPS Data*, Physical Electronics Division, Perkin-Elmer Corporation Eden Prairie, Minnesota, 1992.

This journal is © The Royal Society of Chemistry 2017

J. Mater. Chem. A, 2017, **5**, 24728–24739 | **24739**